MODELING OF SPACE TELESCOPES FOR OBSERVATION OF TRACKS PRODUCED IN THE EARTH'S ATMOSPHERE BY EXTREMELY HIGH ENERGY COSMIC RAYS

D. I. Bugrov[1], G. K. Garipov[2], N. N. Kalmykov[2], B. A. Khrenov[2], M. I. Panasyuk[2], O. A. Saprykin[3], A. A. Silaev[2], D. V. Surogatov[2], V. S. Syromjatnikov[3], I. V. Yashin[2], A. Cordero[4], O. Martinez[4], H. Salazar[4], L. Villasenor[5], A. Zepeda[6], J. Linsley[7]

The main principles of observation of extremely high energy cosmic rays (EHECRs, the primary energy $E_0 > 50$ EeV) with the aid of optical detectors installed in space are considered. Modeling of the space detector response to fluorescence and the Cherenkov light radiated by extensive air showers (EAS) initiated by EHECR helps in designing the TUS and KLYPVE detectors planned to be installed on satellites.

1. Introduction. Scientific goals of the EHECR study. At present, one of the most important and interesting astrophysical problems is the origin of Extremely High Energy Cosmic Rays (EHECRs). Contemporary knowledge of EHECRs and the interest in this problem are based on experimental results obtained with the aid of arrays with large operation area (15 – 100 km^2) that were built between 1959 and 1991 in many countries: Volcano Ranch (USA, 1959), Haverah Park (United Kingdom, 1964), SUGAR (Australia, 1965), Yakutsk (Russia, 1965), Fly's Eye (USA, 1975), and Akeno-AGASA (Japan, 1979, 1991).

The experiments with these arrays showed that the energy spectrum of cosmic rays is extended to energies as high as 10^{20} eV (the first event of energy 10^{20} eV was recorded by the Volcano Ranch array [1] in 1962). The intensity of primary particles of such high energies is very low (it is about one particle per century per 1 km^{2}sr). The accumulation of data with the existing arrays is too slow. The overall statistics of recorded particles of energies higher than 10^{20} eV is about 10; only in three cases (recorded by the Fly's Eye, Yakutsk, and AGASA arrays) the energy exceeded $2 \cdot 10^{20}$ eV. However, even with this low statistics, the existence of the recorded EHE particles and their angular coordinates in the sky is a puzzle for astrophysics.

Immediately after the discovery of the black body radiation in the Universe in 1966, Zatsepin and Kuzmin [2] and, independently, Greisen [3] found that particles with energies higher than $5 \cdot 10^{19}$ eV are absorbed in collisions with photons of the background black body radiation if the distance between the EHECR source and the observer is more than 50 Mps (the GZK effect). Thus, the observed EHECR particles should be accelerated in "local" sources (in our galaxy or in a local cluster of galaxies) whose magnetic fields are weak enough to deflect primary protons; therefore, the observed directions of EHE particles should indicate their source. Attempts to find a correlation between arrival directions of experimental events and various kinds of astrophysical sources [4 – 6] did not yield a confident identification of local sources. Hillas's diagram [7] specifies a possible EHECR source as a site capable to confine particles of energy higher than 10^{20} eV. Among "local" astrophysical objects, quite a few could be EHECR source candidates.

This puzzle could be solved if "exotic" sources of the fundamental super heavy (10^{24} eV) GUT particles (the "topology defects" of the Universe) are introduced to explain the observed events (see a review in [8]). The GUT particles emitted from those sources decay to hadrons, leptons, and photons of much lower energies — down to 10^{20} eV. Theoretically, photons are the most probable particles that could be observed. In this scenario, the isotropic distribution of arrival directions is expected, since there is no specific prediction for the topological defect distribution in the Universe (the distance to a source has still to be "small", < 50 Mps, due to the GZK effect).

[1] Faculty of Mechanics and Mathematics, Moscow State University, Moscow, 119899, Russian Federation, e-mail: valex@moids.math.msu.ru; bugrov@moids.math.msu.ru

[2] Skobeltsyn Institute of Nuclear Physics, Moscow State University, Moscow, 119899, Russian Federation, e-mail: garipov@eas.npi.msu.ru; kalm@eas.npi.msu.ru; khrenov@eas.npi.msu.ru; panasyuk@srdlan.npi.msu.ru; yashin@eas.npi.msu.ru; silaev@eas.npi.msu.ru

[3] Rocket Space Corporation "Energia" (RSC "Energia"), Consortium "Space Regatta", Korolev, 141070, Moscow Region, Russian Federation

[4] Facultad de Ciencias Fisico Matematicas, Universidad Autonoma de Puebla, Apdo. Postal 1364, Puebla, México, e-mail: cordero@fcfm.buap.mx; omartin@fcfm.buap.mx; hsalazar@fcfm.buap.mx

[5] Instituto de Física y Matemáticas, U. Michoacan, A. Postal 2-82, 58040, Morelia Michoacan, Mexico, e-mail: villasen@zeus.ccu.umich.mx

[6] Depto de Física, Cinvestav-IPN, 07000, Mexico D. F., Mexico, e-mail: zepeda@fis.cinvestav.mx

[7] Department of Astronomy and Physics, University of New Mexico, 800 Yale Bullevard, N.E., Albuquerque, New Mexico, 87131, USA, e-mail: jlinsley@as.unm.edu

Only particles of weak interaction (neutrino or hypothetical supersymmetric particles) may reach an observer from cosmological distances ($\gg$ 100 Mps). At the same time, the interaction cross section of those particles should be high enough to produce an observable EAS in the atmosphere. Neutrino is a possible candidate for a "cosmological" EHE particle. It is expected that the neutrino-nucleus cross section at energies 10^{20} eV is only 1000 times less than the proton-nucleus cross section [9]. The neutrino-induced EAS should develop deeper in the atmosphere than proton showers; this makes a distinct "signature" of EHE neutrino events. If neutrino EHE events are discovered, then the cosmological sources of EHECRs can be studied straightforward: the direction of a neutral neutrino indicates the source and the GZK effect does not limit the distance to the source. In the case of neutrino detection, the limitation comes from the fact that, in any kind of EHECR sources, neutrino is a secondary particle: it is either a product of decay of the particles produced during EHE hadron interactions or a product of decay of the GUT particles. During the hadron interactions, neutrinos get only a 1/20 fraction of the primary particle and, for the effective detection of EHECRs (the energy $> 5 \cdot 10^{19}$ eV) via neutrino, the energy threshold has to be low (of about $0.05 \cdot 5 \cdot 10^{19}$ eV $= 2.5 \cdot 10^{18}$ eV).

In order to solve the above fundamental problem, experimental arrays of gigantic geometrical factor S (km^2) Ω (sr) multiplied by the duty cycle T (years) are needed ($S\Omega T > 10^5$ km^2 sr years). Recently, several projects of large land-based detectors have been suggested: EAS-1000 [10]; HIRES [11], Pierre Auger Observatory [12, 13], Telescope Array [14]. The most adequate installation to be built is suggested by the Pierre Auger Observatory collaboration: two arrays in both the Earth's hemispheres with $S\Omega = 3000$ km^2 sr each and with the field of view covering the whole sky. In 10 – 20 years of operation, this array is expected to solve the problem.

There is another approach to the problem: to use as larger area of the atmosphere surface as possible during comparatively short observations (less than five years) with the aid of instruments observing EHECR signals from Earth satellites. Being suggested by Linsley [15, 16] in 1981, this original idea was developed in the framework of several projects (in particular, it is planned to mount a EHECR detector on the Russian segment of the International Space Station [17, 18]).

In this approach, a fluorescence track of the shower initiated by a EHE primary particle in the atmosphere is observed from space ("downward"), as performed on the Earth's surface by the Fly's Eye array. In observations from a satellite orbit (from a distance R to the Earth's atmosphere), an optical detector with a field Ψ of view will observe a large atmosphere area $S \approxeq (R \tan \Psi)^2$ due to the large distance R. Estimates of energy thresholds for observations from a distance R of 400 – 500 km with a camera using a mirror of diameter 3 m show that the threshold energy is about 10^{19} eV. For energies $E \approxeq 10^{19}$ eV, the EHECR intensity is large enough for effective observations with a "telescope" of a comparatively narrow field of view (FOV) — of about 15 degrees. With this FOV, the observation area is $S = 10^4$ km^2 and the statistics of EHECR events per year is thousands of events even for a telescope duty cycle of 20 %. The FOV of 15 degrees is characteristic for a simple optics of the parabolic mirror detector. To make the area S larger, either the FOV should be increased (a more complicated optics for wide FOV detectors has to be developed) or a satellite orbit should be higher. These two options are the two directions of the space EHECR detector development: detectors of the OWL type [19, 20] and detectors of the "telescope" type [21, 22].

In the telescope option, the mirror area could be constructed larger than an aperture in the OWL option. In the telescope case, the threshold energy of about 10^{18} eV at a distance R of 400 km could be achieved with a mirror area of about 400 m^2 and the efficiency of the EHECR detection including EHE neutrinos is high. With a large telescope mirror area (400 – 1000 m^2), particles of the highest energies of about 10^{21} eV could be studied from an orbit of radius $R \approxeq 36000$ km in an area $S \approxeq 10^7$ km^2 (almost the entire area of the Earth's disc) [22].

Thus, the general trend of EHECR space observations is to start measurements at orbit heights close to 400 km, checking new results at energies 10^{19} – 10^{20} eV in comparison with the existing results from the land-based arrays, and then to develop more complicated detectors (telescopes with large mirror area at high orbits and/or wide FOV detectors) so that the geometry factor of the instruments would be much higher — of the order of the Earth's atmosphere area.

The Kosmotepetl collaboration has chosen the telescope option of the space EHECR detector development. The collaboration program is to start measurements with a small telescope prototype (the mirror area 1.4 m^2) launched as an additional payload on one of the commercial satellites (the TUS project), then to design and construct a telescope with the mirror area 10 m^2 capable of measuring EHECRs, starting from an energy of 10^{19} eV. This telescope could be mounted on the Russian segment of ISS (the KLYPVE project). During two–three years of operation at ISS, the KLYPVE telescope will perform the study of EHECRs over the energy range 10^{19} – $5 \cdot 10^{20}$ eV. The results obtained over this period will allow us to check various scenarios for the origin of EHECRs and to plan the next steps in the space observations of EHECRs.

The experience in construction and operation of TUS and KLYPVE telescopes will allow us to design

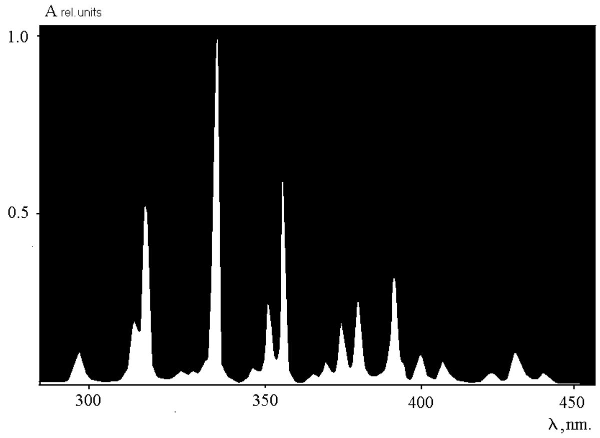

Fig. 1. The fluorescence light spectrum

bigger mirrors (of hundreds m^2 in area) and to launch special devices at orbits of $R = 400 - 600$ km in height for studying EHECRs of low energy threshold ($2 \cdot 10^{18}$ eV, neutrino-induced events included). A telescope with a mirror area of hundreds m^2 will allow us to observe EHECR events from geostationary orbits ($R \approxeq 36\,000$ km), covering almost the entire Earth's atmosphere.

Modeling of the telescope performance in space is an important stage of the Kosmotepetl collaboration program. Here we present physical principles of the EHECR detection by a space telescope and the first results on modeling the TUS and the KLYPVE telescopes.

2. Method of observation of the extremely high energy primary particles as fluorescent tracks in the Earth's atmosphere. A EHE particle at collision with air nuclei produces hadrons that, in their turn, collide with air nuclei; an extensive air shower (EAS) starts to develop in the atmosphere. Among generated secondary particles, there are neutral pions (and kaons) that decay to photons, initiating the electromagnetic shower. The most numerous charged particles in this complex hadron-electromagnetic cascade are electrons (positrons). The number of electrons (the size N_e of the shower) in the cascade maximum is in proportion to the primary energy E_0: $N_{e\,\max} \approxeq E_0/1.3$ (E_0 in GeV).

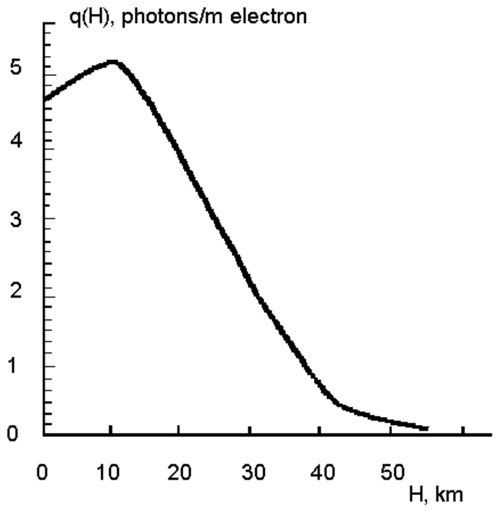

Fig. 2. The fluorescent light yield q per electron per m as a function of height H in the atmosphere (for the "standard atmosphere")

Shower electrons (and other charged particles), moving through the atmosphere, ionize air atoms and excite unstable electron levels in air atoms and molecules. After a short relaxation time, electrons from those levels return to the atom (molecule) basic levels, emitting the characteristic light — a fluorescence light. The light

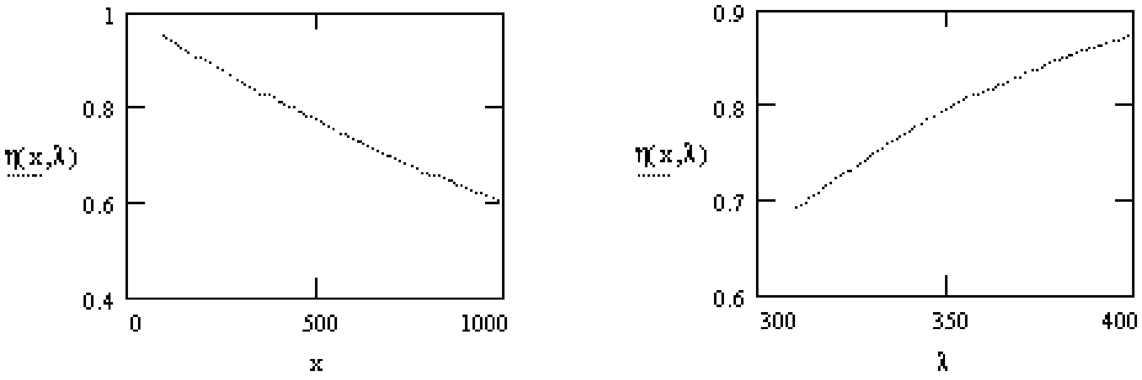

a *b*

Fig. 3. The fraction of the fluorescent light escaped the extinction due to the Rayleigh scattering: *a*) as a function of atmosphere depth X (the average wavelength $\lambda = 360$ nm), *b*) as a function of wavelength λ (for the atmosphere, $X = 400$ g/cm^2).

from excited molecules of nitrogen with peaks at wavelengths from 310 up to 420 nm (Figure 1) is the most effective fluorescence light in air. The yield of the fluorescent light depends on the air density and temperature, but fortunately it is almost constant in a wide range of heights in the atmosphere (Figure 2) and is equal to 4.5 – 5 photons per electron per meter of its path.

The emitted light is isotropic and is in proportion to the shower size at a given depth in the atmosphere. On the route to the detector, the fluorescent light goes out of the beam by the Rayleigh scattering and by the Mia (aerosol) scattering. The Rayleigh scattering light absorption path X_R g/cm^2 is equal to

$$X_R(\lambda) = 2974\,(\lambda/400)^4 \tag{2.1}$$

and the fraction of the fluorescence light detected at a "distance" of X g/cm^2 from the shower disc is

$$\eta(\lambda) = \exp\big(-X/X_R(\lambda)\big) \tag{2.2}$$

The coefficient η is shown in Figure 3 as a function of X and λ.

The width of the EAS disc is much less than the length of the whole cascade (for example, the length of the cascade developing at zenith angles $\theta = 0° - 30°$ is about 10 km and the width of the disc at sea level is about 0.1 km). The event recorded in the detector looks like a point light spot moving along the shower trajectory in which the recorded amount of light is in proportion to the shower size N_e. The integral of light recorded in the track (as well as the light signal at the shower maximum) is in proportion to the primary energy E_0. The recorded cascade shape (especially the position $X_{\max}$ of a shower maximum in the atmosphere) allows us to distinguish various origins of the primary particle (photon, proton, or nucleus).

The difference in a position of the shower maximum expected for the proton and heavy nuclei showers is shown in Figure 4 (Curves 2 and 3). The experimental data [23] at energies of about 10^{19} eV are represented in this figure with points.

As mentioned above (Section 1), the distinction between primary photons and hadrons (protons and nuclei) is of special interest. In the development of the cascade initiated by extremely high energy photons, the "photon" shower differs from the hadron shower by the two effects:

1. the Landau–Pomeranchuk–Migdal (LPM) effect of decreasing the photon cross section for the pair production in air at energies more than $3 \cdot 10^{19}$ eV;

2. the enlarged cross section of the pair production in the geomagnetic field at energies more than $5 \cdot 10^{19}$ eV.

Recently it has been noticed (see, for example, [24, 25]) that photons crossing the geomagnetic field of the transverse magnetic field $B_t \gg 0.2$ Gauss at energies more than 10^{20} eV produce an electromagnetic cascade before entering the Earth's atmosphere, so that the energies of photons and electrons initiating an electromagnetic cascade in the atmosphere are of hundreds times lower than the primary photon energy. The resulting cascade in the atmosphere is "normal" (i.e., without the LPM effect). Photons coming to the atmosphere along the geomagnetic field ($B_t \ll 0.2$ G) produce the cascade as the LPM effect predicts — developing deep in the

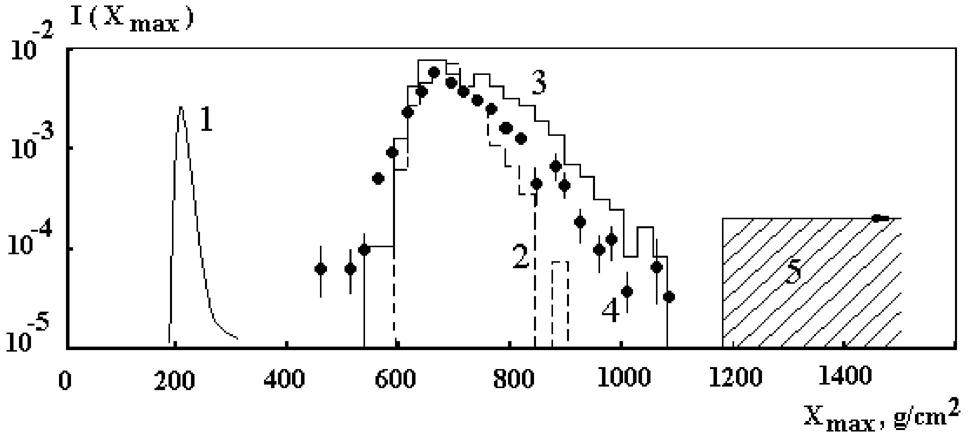

Fig. 4. The distribution of positions of the shower maximum $X_{\max}$ for primaries of different origin: 1 — the relativistic dust grain, 2 — proton, 3 — iron nucleus, 4 — the experimental data from the Fly's Eye array, 5 — neutrino

atmosphere. The difference in the "photon" cascades developing across and along the geomagnetic field is represented in Figure 5 (the results of calculations from [26]). In hadron showers, the energy of photons initiating the electromagnetic part of the shower is hundreds times less than the primary energy and, at primary energies of about 10^{20} eV, the LPM effect does not start yet [27]. The shape of the cascade curve in the hadron showers is close to that of the photon showers developing across the geomagnetic field (Figure 5).

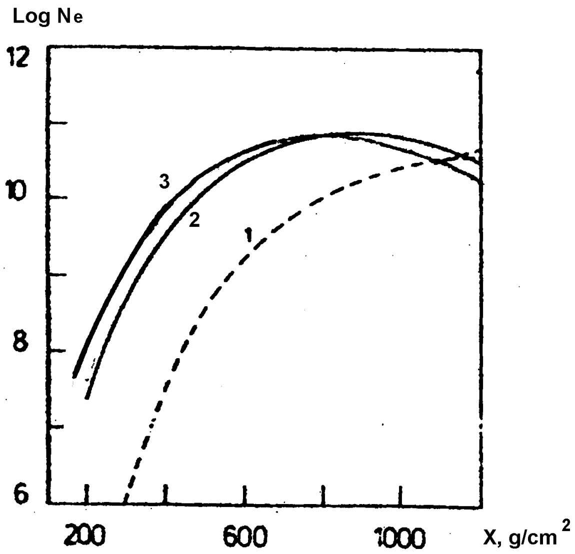

Fig. 5. The cascade curves of showers of energy $E_0 = 10^{20}$ eV initiated by: 1 — photon passing along the geomagnetic field (the LPM effect is valid), 2 — photon passing across the geomagnetic field, 3 — proton (independent of the geomagnetic field)

Observing the showers initiated by particles going along the geomagnetic field, we can distinguish the photon shower as a shower with its maximum much deeper in the atmosphere than in a hadron shower. Observations from satellites have the advantage of a wider range of the Earth's magnetic field directions than at a fixed site on the Earth.

The shapes of the cascade curve in the "exotic" case of the shower initiated by a relativistic dust particle are expected to be quite different. It was suggested long ago [28] that relativistic dust grains can produce showers of extreme energies. The dust particle acceleration by a radiation flux in Super Nova (SN) explosions was introduced in [29]. Survival of highly relativistic dust particles in a high density radiation flux was doubtful [30], but recently [31] it was shown that a dust particle with the Lorentz factor $\leqslant 10$ survives. The dust grain could be accelerated by radiation from the SN shock wave and a relativistic dust flux could be detected at the Earth as the dust "burst".

The dust grain having the Lorentz factor of about 10 and the number of nucleons $A = 10^{10}$ will produce a shower of total energy 10^{20} eV. Figure 6 shows the "dust" cascade curve calculated according to the principle of superposition of A showers produced by nucleons of energy E_0/A. This is in sharp contrast with the cascade curve of hadron showers (Figure 4). It should be noted that the "dust" electron shower is easily detected by a space detector, but it is hard to detect it by a land-based array. This array can only detect the muon component of the dust shower that contains much less particles.

The dust SN burst hypothesis [31] poses an interesting problem for the space detector: a search for dust bursts correlated with other SN phenomena.

Another exotic cascade curve shape appears in showers initiated by neutrinos: electron, muon, or tau neutrinos. All neutrino showers are expected to start deeply in the atmosphere, since the "neutrino-air nuclei" cross section is much lower than the "proton-air nuclei" cross section. The shower initiated by electron neutrino is close in shape to a photon or hadron shower. The electron neutrino showers are distinguished from the photon and hadron showers only statistically — as showers initiated deeply in the atmosphere. The muon neutrino or tau neutrino showers might be different from "standard" showers. It is expected [32] that their cascades might have several maxima produced by electromagnetic showers initiated deeply in the atmosphere by high energy muons or tau particles having small interaction cross sections with air nuclei.

The expected distribution of $X_{\max}$ in events initiated by different primary particles is presented in Figure 4. Relativistic dust grains will produce showers with their maxima at "shallow" depths of about 200 g/cm^2, hadrons — at depths of 400 – 1000 g/cm^2, and neutrinos — at depths > 1500 g/cm^2.

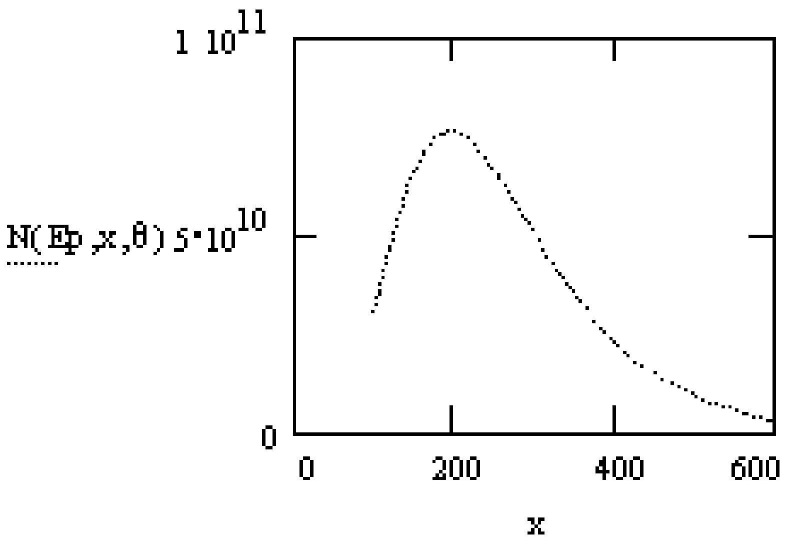

Fig. 6. The cascade curve in the "dust" shower. $E = 10^{20}$ eV, the number of nucleons is 10^{10}, the nucleon energy is 10 GeV, the atmosphere depth X is given in g/cm^2

Let us consider the light signal from an EAS track at an optical satellite-borne detector in greater detail. There are several advantages in "downward" observations from the satellite in comparison with "upward" observations from the Earth's surface:

— one detector covers a large area in the atmosphere,

— event selection criteria are uniform over this area,

— the air transparency in "downward" observations is higher than in a horizontal direction at the Earth's surface,

— the detection efficiency for near-horizontal tracks (the zenith angles $\theta > 60°$) is higher, the air transparency for those tracks is very high and constant,

— near-horizontal tracks are above the clouds and their observation has the duty cycle 2 – 3 times higher than at the Earth's surface,

— the detection efficiency is uniform in a wide range of $X_{\max}$; therefore, a search for the "exotic" showers from dust grains and neutrinos is highly efficient.

A fluorescence signal (the number of photons with wavelengths $\lambda = 310$–420 nm) from a shower track interval ΔL is in proportion to the EAS size $N_e(H,\theta)$ at height H in the atmosphere from the EAS with the zenith angle θ:

$$Q(H,\theta) = N_e(H,\theta)\, q(H)\, \Delta L\, \eta(H)\, S/4\pi R^2 \quad \text{photons} \tag{2.3}$$

Here the factor $q(H)$ is the yield of the fluorescence light in photons per meter per electron (Figure 2), $\eta(H)$ is the fraction of the fluorescence light survived in scattering processes (for the Rayleigh scattering, $\eta(H)$ is given in Figure 3), S is the telescope mirror area, and R is the orbit height above the Earth's sea level. Since $H \ll R$, we can ignore H in our estimates for the distance $R - H$ between the detector and the EAS track.

The EAS size (as a function of the primary particle energy, atomic number, and direction) is available from the model calculations. In order to estimate the fluorescence detector properties, we will use the formula suggested by Iljina and Kalmykov [33]. This formula approximates the results of the EAS calculation in the QGSJET model for proton primary:

$$\begin{gathered} N_e(E_0,x,\theta) = E_0/1.3 \exp\big(t(x,\theta) - T(E_0) - 2t(x,\theta)\ln\left(s(E_0,x,\theta)\right)\big) \\ T(E_0) = 0.8\ln\left(E_0/0.81\right), \quad t(x,\theta) = x/t_0\cos\theta - 1.842 \\ s(E_0,x,\theta) = 2/\big(1+T(E_0)\big)/t(x,\theta) \end{gathered} \tag{2.4}$$

Here t_0 is the radiation unit in g/cm^2, E_0 is the primary energy in GeV, and x is the depth in the atmosphere at the track position x.

Here the absolute depth of the EAS maximum is 700 g/cm^2 for the primary energy 10^{10} GeV. The fluctuation of a maximum position in the shower-to-shower analysis may be introduced in the factor $t(x,\theta)$ by the additional parameter Δt. The cascade initiated by a primary particle with atomic number A is well presented by the superposition of A cascades initiated by protons with energy E_0/A.

To convert the cascade to geometrical path units (as needed in formula (2.3)), one has to use an atmosphere model, for example, to use the relation

$$H = 6.8\ln\left(1020/x\right), \quad H \text{ in km} \tag{2.5}$$

Some parameters of tracks corresponding to the primary proton energy $E_0 = 10^{19}$ eV and to various values of the zenith angle θ are given in Table 2.1: the shower maximum height $H_{\max}$, the track length $L_{1/2}$ at the level of size $N_e = N_{e\,\max}/2$, the visible track length $L'_{1/2}$, the track width $D_{1/2}$, and the expected track duration in the detector $T_{1/2}$. It is assumed that all the showers have their positions of maximum in the atmosphere at a depth of 700 g/cm^2.

Table 2.1

θ	80°	75°	70°	65°	60°	30°
H_m, km	20	14	11.5	10	9	4.5
$L_{1/2}$, km	37	25	19	15	13	7
$L'_{1/2}$, km	36	24	18	13.5	11	3.5
$D_{1/2}$, km	1	0.65	0.5	0.45	0.4	0.2
$T_{1/2}$, μs	150	110	90	70	65	45

It follows from Table 2.1 that the tracks with zenith angles more than 60° are longer than $L_{1/2} = 13$ km, their maxima are higher than 9 km, and their duration $T_{1/2}$ is longer than 65 μsec. The track of width $D_{1/2}$ is equal to the Moliere diameter of the shower particle disc at a given height in the atmosphere. At all zenith angles, this width is much less than the track length. For a reasonable detector angular resolution Δ of about 5 mrad, the disc size could not be resolved at orbits higher than 400 km. Analyzing a shower disc image, we consider it as a point moving along a straight line.

The detector pixels divide the track length by intervals $\Delta L = \Delta \cdot R$. At zenith angles of about 80°, the pixel size $\Delta = 5$ mrad corresponds to the atmosphere depth interval 40 g/cm^2. The pixel depth interval increases with decrease in the zenith angle. Due to a possible observation of the temporal profile of the EAS signals, the resolution of the cascade maximum could be high even at small zenith angles (see below).

Considering the shower tracks in the optical detector, we should take into account not only the fluorescence light but also the Cherenkov light from electrons moving with velocities higher than the light velocity in air. In contrast to fluorescence light, the Cherenkov light is collimated in the direction of a primary particle (the half of the Cherenkov light is emitted at angles $\Psi_{\rm ch} < 0.05$ rad to the direction of the primary particle). The yield of the Cherenkov light emitted from a track interval Δx (g/cm^2) in the wavelength range $\lambda = 310$ – 420 nm is equal to

$$Q_{\rm ch}(E_0, x, \theta) = N_e(E_0, x, \theta)\, q_{\rm ch}\, \varepsilon(x)\, \Delta x \tag{2.6}$$

where $q_{\rm ch}$ is the Cherenkov light yield per electron per g/cm^2 ($q_{\rm ch} = 287$ photons per g/cm^2), $\varepsilon(x)$ is the fraction of EAS electrons with energy above the Cherenkov radiation threshold ($\varepsilon = 0.3$ at sea level). The integrated flux of the Cherenkov light at the depth X is equal to

$$Q_{\rm ch}(X, \theta) = \int\limits_0^X Q_{\rm ch}(E_0, x, \theta) \exp\big((X - x)/X_{R+Mi}\big)\, dx \quad \text{photons} \tag{2.7}$$

Here the exponential factor takes into account the absorption of the Cherenkov light in air due to the Rayleigh–Mie scattering. The integral Cherenkov light flux is in proportion to the primary energy, for example, for a vertical shower at sea level:

$$Q_{\rm ch} \approxeq 3 \cdot 10^{14}\, (E_0/10^{19}) \quad \text{photons} \tag{2.8}$$

When passing through the atmosphere, the Cherenkov light continuously scatters at air molecules and aerosol, but when meeting a "solid" surface of clouds, sea or ground, it locally scatters back (or absorbed). Both types of the scattered Cherenkov light are detected by a telescope.

The scattered Cherenkov light detected in air may be presented as

$$Q_{\rm chsc}(E_0, X, \theta) = Q_{\rm ch}(E_0, X, \theta)\, \Delta X / X_{R+Mi} S (1 + \cos^2\delta)/4\pi R^2 \tag{2.9}$$

where δ is the angle between the direction of the track and the direction from the point of scattering to the telescope, ΔX is the track interval observed in a pixel. Our comparison of the luminescent light flux calculated by formulas (2.3) – (2.5) with the scattered Cherenkov light calculated by (2.9) shows that the scattered Cherenkov light is small in comparison with the fluorescent light coming from the shower maximum. However, when the cascade is far beyond the maximum, the scattered Cherenkov light might be comparable with the fluorescent light. The yield of the scattered Cherenkov light depends on the air density; the shape of the registered cascade curve is different for different levels of depth in the atmosphere. This effect might be useful for the separation of neutrino-induced showers (see below, Section 4).

The Cherenkov light scattered on a solid surface at a height $H_{\rm RChS}$ produces a Reflected Cherenkov Spot (RChS) in the telescope. The RChS is recorded as a signal equal to

$$Q_{\rm RChS} = k\, \eta(H_{\rm RChS})\, Q_{\rm ch}(E_0, X(H_{\rm RChS}), \theta) S / 2\pi (R - H_{\rm RChS})^2 \tag{2.10}$$

where k is the "albedo" coefficient of the surface and η is as above in formula (2.3).

The RChS looks like an ellipsoid with a long axis "$a_{1/2}$" and a short axis "$b_{1/2}$" (the subscript 1/2 indicates that half of the reflected light is contained inside the ellipsoid with the dimensions "a" and "b"). These axes are represented in Table 2.2 for various values of the zenith angle.

Table 2.2

θ	30°	60°	70°	80°
$a_{1/2}$ km	0.23	1.6	4.5	25
$b_{1/2}$ km	0.20	0.8	1.5	4.3

The values given in Table 2.2 were calculated as

$$a_{1/2} = \Psi_{\rm ch\,1/2} H_{\max}/\cos\theta \quad \text{and} \quad b_{1/2} = \Psi_{\rm ch\,1/2} H_{\max}/(\cos\theta)^2 \tag{2.11}$$

At zenith angles $\theta < 70°$, the RChS is detected in one or two pixels and its duration is about $500/\cos\theta$ nsec. At zenith angles $\theta > 70°$, the spot is very wide (Table 2.2), the RChS may go out of the telescope FOV and the detection of the RChS is less probable.

The presence of a RChS in a shower track makes it possible to measure the absolute track depth in the atmosphere. By an additional control measurement, the height of the reflective surface could be determined with a high precision (see below the section on control measurements) and a position of the RChS becomes a reference depth in the atmosphere for the whole shower track (including a position of the shower maximum $X_{\max}$). This method of determining $X_{\max}$ is relevant both in geometrical analysis of the "hit" pixels and in an analysis of temporal profiles of track signals (the RChS pulse is separated from the fluorescence track pulse by some time interval).

3. The signal-to-noise ratio in the KLYPVE and TUS detectors. The estimation of signals (and noise) were made mostly for the KLYPVE detector planned to be launched to the Russian segment of ISS. Below we also consider signals in a prototype detector — the TUS detector. The parameters of the KLYPVE and TUS detectors are presented in Table 3.1

Table 3.1

Detector	**KLYPVE**	**TUS**
Orbit height, km	400	350–600
Mirror operating area, m^2	10	1.4
Focal distance, m	3	1.5
Pixel angular size, mrad	5	7.5
Detector FOV, rad	0.25×0.25	0.12×0.12
Pixel number	2500	256

As a first estimate, the signal in a pixel registering the EAS maximum size is of prime interest. This signal is selected by the detector triggering system and determines the energy threshold of the detector. Pixel signals in a number of PM tube photoelectrons were calculated in the EAS maximum as

$$q_m(E_0, \theta) = Q_m(E_0, \theta)\, p \tag{3.1}$$

where $Q_m(E_0, \theta)$ is the photon flux density from the EAS maximum at an orbit of height R calculated with the aid of formulas (2.3), (2.4) and p is the PM tube quantum efficiency (in our estimates, $p = 0.2$).

Results for the KLYPVE and TUS detectors are presented in Table 3.2 for various values of the zenith angle and primary energies.

Table 3.2

KLYPVE detector

Zenith angle	80°	70°	60°	30°
$q_m(E_0 = 10^{19}$ eV$, \theta)$, p.e.	81	76	78	115
$q_m(E_0 = 3 \cdot 10^{19}$ eV$, \theta)$, p.e.	243	228	234	345

TUS detector

Zenith angle	80°	70°	60°	30°
$q_m(E_0 = 10^{19}$ eV$, \theta)$, p.e.	18	16	17	24
$q_m(E_0 = 3 \cdot 10^{19}$ eV$, \theta)$, p.e.	54	48	51	72

The previous space measurements yielded the amount of the noise expected in camera pixels at a night side of the Earth for orbits of height $R = 200 - 600$ km. The average intensity of light in the wavelength band of the UV-1 filter ($\lambda = 260 - 400$ nm) at the Cosmos 45 satellite ($R = 200$ km) was shown [34] to be in the range of 200–600 photons/m^2 ns sr. One of the Cosmos 45 measurements during moonless nights in a region of ocean is represented in Figure 7.

The light intensity measured in the visual band $\lambda = 400 - 600$ nm is also shown in Figure 7. Variations in intensity are correlated with a cloud cover. The light intensity in the visual band is approximately 10 times higher than in the UV band. The authors of [34] noted that in the UV band the correlation with clouds is

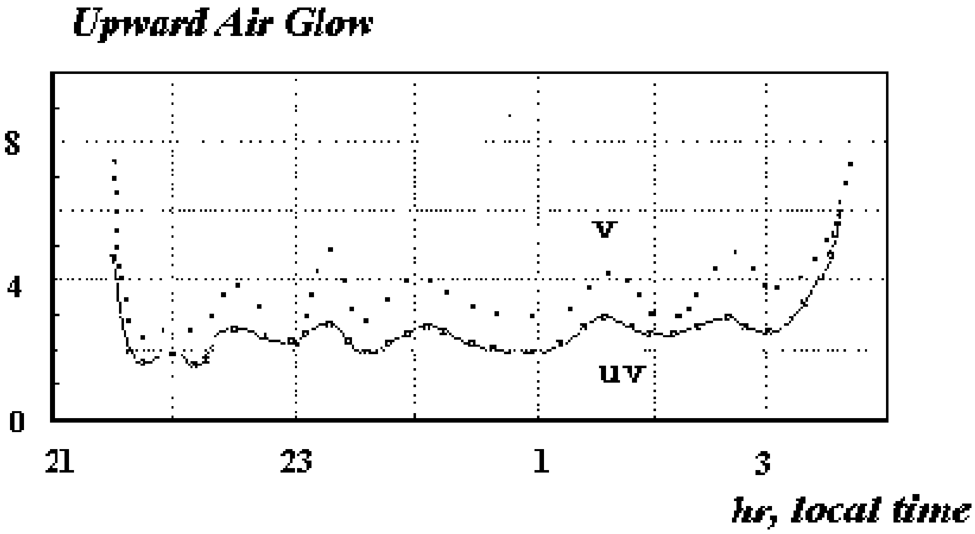

Fig. 7. The intensity of the night atmosphere glow as measured in the COSMOS 45 experiment. The solid line — the wavelength range 260 – 400 nm, the intensity units are 10^2 photons/m^2 sr ns. The dotted line — the visual range 400 – 600 nm, the intensity units are 10^3 photons/m^2 sr ns.

less than in the visual light. The lowest intensity of about 200 photons/m^2 ns sr corresponds to the clearest (cloudless) regions and should be compared with the surface "downward" sky light intensity. In a simple estimate of the "upward–downward" (u/d) intensity ratio due to the molecular scattering (only) a u/d ratio of ≈ 0.7 should be expected in the UV band (320 – 400 nm) and the upward intensity 200 should be converted to the downward intensity 300 photons/m^2 ns sr, which agrees with the experimental figures at clear atmosphere sites where the surface fluorescence detectors were used [35].

During moon nights, the light intensity is higher due to the scattered back moon light. The scattered light intensity is represented in Figure 8 for various moon phases. During the satellite circuit, the moon elevation is changing as well as the scattered light intensity. For the full moon and an elevation of 90°, the light intensity is in maximum and is equal to $3 \cdot 10^4$ photons/m^2 ns sr (over the wavelength range 310 – 420 nm).

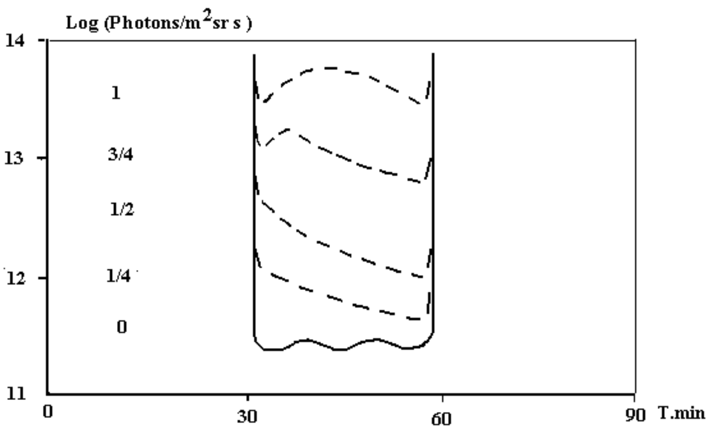

Fig. 8. The intensity of the scattered moon light for various moon phases. The moon phase is indicated on the curves

The average duty cycle of the detectors during moonless nights is about 6% and during moon nights is about 16 % (6 % with full moon), the duty cycle of all nights is 22 % of that for the day.

The human-made light intensity should be checked in new experiments, but the duty cycle of measurements above big cities is expected to be no more than 1/5 of the night duty cycle (4 % of the day).

In atmosphere regions with a light intensity ν (photons/m^2 ns sr), the noise in camera pixels (in number of photoelectrons) is equal to the RMS of the average photo electron number:

$$\sigma = \sqrt{\nu p S \omega \Delta t} \ \text{p.e.} \tag{3.2}$$

Here Δt (ns) is the time interval of signal observation in one pixel and ω is the pixel solid angle.

The atmosphere glow during moonless nights ($\nu = 200$ photons/m^2 ns sr), during an average moon night ($\nu = 3000$ photons/m^2 ns sr), and during full moon nights ($\nu = 3 \cdot 10^4$ photons/m^2 ns sr) is responsible for the noise in pixels of the KLYPVE and TUS detectors. In Table 3.3, the time interval Δt is chosen to be equal to the signal duration of horizontal tracks ($\Delta t = 7000$ ns in the KLYPVE detector and $\Delta t = 14000$ ns in the TUS detector).

Table 3.3

Detector	KLYPVE	TUS
Moonless night	8.4 p.e.	6.6 p.e.
Average moon night	32.5 p.e.	25.5 p.e.
Full moon night	102 p.e.	80 p.e.

Comparing the values of signals given in Table 3.2 for near-horizontal tracks ($\theta \geqslant 60°$) with the noise given in Table 3.3, one can find the first estimate of the energy threshold for the KLYPVE and TUS detectors that observe EHECR events above the clouds. The values of the energy thresholds $E_{0\ \text{thr}}$ are shown in Table 3.4 for the KLYPVE and TUS detectors when the signal threshold equals 5σ of the noise. For the solid angle of the EAS registration at zenith angles $\theta \geqslant 60°$ taken equal to 3 sr, the atmosphere area for the EAS registration equals 10^4 km^2 for the KLYPVE detector and equals $3.6 \cdot 10^3$ km^2 for the TUS detector. Assuming that the duty cycle for various night conditions is taken as mentioned above, the cosmic ray intensity is 0.8 event/km^2 year sr for $E_{0\ \text{thr}} = 10^{19}$ eV and the integral exponent γ of the spectrum is equal to 1.75, we can find the event rate per year (see Table 3.4).

Table 3.4

KLYPVE detector

Night condition	$E_{0\ \text{thr}}$, eV	Event rate per year
Moonless	$5 \cdot 10^{18}$ eV	6000
Average Moon	$3 \cdot 10^{19}$ eV	560
Any night	10^{20} eV	94

TUS detector

Night condition	Energy $E_{0\ \text{thr}}$, eV	Event rate per year
Moonless	$2 \cdot 10^{19}$ eV	150
Average Moon	$7.7 \cdot 10^{19}$ eV	40
Any night	$2.3 \cdot 10^{20}$ eV	8

Another source of noise is the Cherenkov and fluorescence light produced by charge particles passing through optical elements of the photo receiver (PM tube glass, UV filter, etc.). These noise signals are very fast (ns) and, in special cases (heavy CR nucleus producing fluorescence in glass), could initiate big charges in PM tubes. The charge particle flux from the Earth's radiation belts is comparatively low at low orbits ($R < 600$ km), but when planning a trigger system of the space detector, one should be aware of the intensity of fast signals from cosmic ray and "albedo" particles.

For the ISS orbit (400 – 500 km), the intensity of albedo electrons of energy more than 2 MeV (producing of about 10 – 20 p.e. in the detector pixel by radiating the Cherenkov light in a UV-filter of thickness 4 mm)

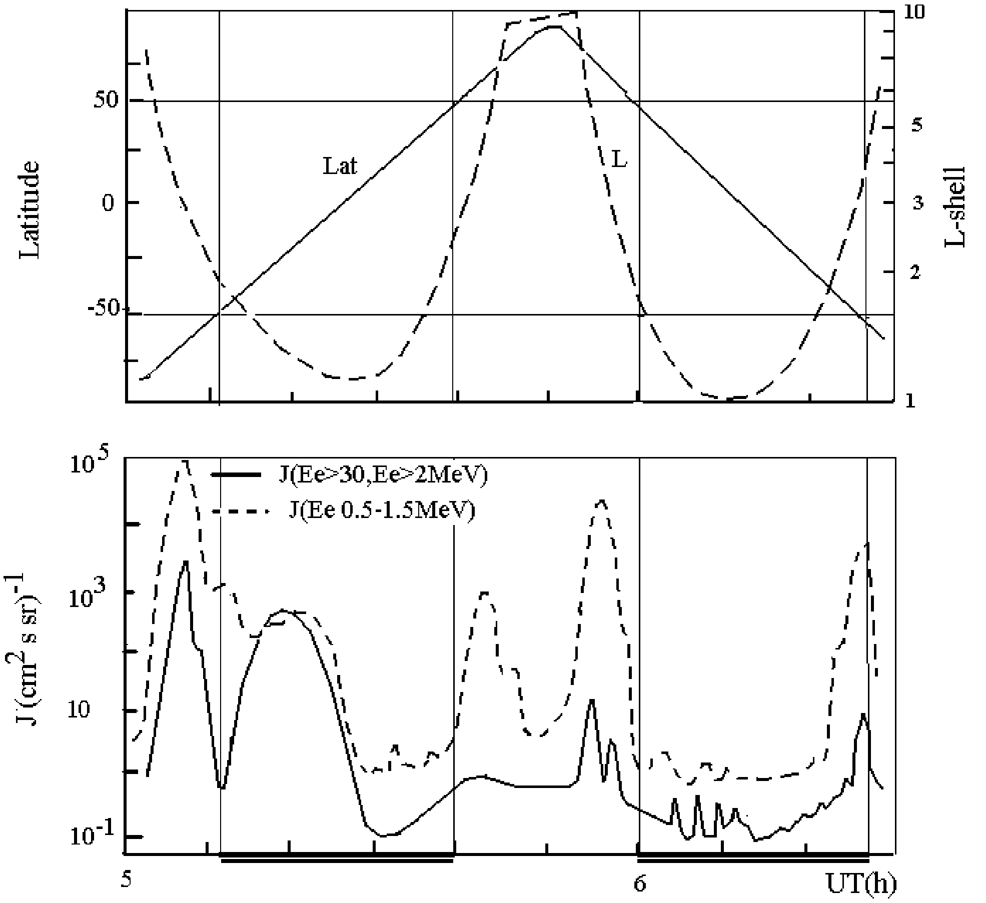

Fig. 9. The intensity of cosmic ray and albedo particles as a function of time UT; the ISS orbit hours are indicated by the solid lines. The correlation of time, L-shell, and latitude are shown in the upper part of the figure

is higher than the intensity of galactic cosmic ray particles (producing the same signals) as was shown in [36]. Data [36] on the intensity of albedo particles as a function of L-shell or latitude are shown in Figure 9.

In the southern hemisphere, the orbit crosses the Brazilian anomaly, where the electron intensity is of four order in magnitude higher than in "quiet" regions. At high latitudes, the ISS orbit slightly touches the radiation belt (Figure 9). Fast signals from cosmic ray particles do not essentially affect the triggering system and the pixel data on EHECR fluorescence tracks, but they are important for interesting experiments suggested to search for the tau-neutrino signals that come from the Earth (Takahashi, [20]) and produce the Cherenkov light directed to the camera (fast signals). Estimates of signals from the neutrino-induced direct Cherenkov light (in comparison with the rate of albedo particle signals) show that the separation of upward tau neutrino from the noise is reliable only in two-fold coincidences of two space optical detectors (KLYPVE+EUSO).

4. Control measurements of height H_{RChS} and atmosphere parameters in the detector FOV. Measurements of the height H_{RChS} (the height of surface "reflected" the shower Cherenkov light) can be made with the aid of the same detector observing a scattered back signal from a control light flasher triggered immediately (for example, in 1 ms) after the reception of the EHECR event when a position of a space station was not changed yet. In 1 ms, a position of the space station will change only by 8 m (i.e., a map of reflecting surface will be exactly the same as in the EHECR event). For this aim, in the KLYPVE and TUS detectors the flash lamp will be installed. As a response to the signal from the registered EHECR event, the lamp makes a flash with its duration equal to the pixel time resolution (200 ns). In a period of time needed for the light to pass the distance $R = 400$ km and back (2.6 ms), there will be a region of signal scattered back: in the air Rayleigh scattering, in the scattering from "reflective" semitransparent high clouds, from the cloud cover, and from ground or sea.

The accuracy in pixel time measurements (200 ns) ensures a high accuracy in measurements of the distance between a telescope and a reflective media: the errors are about 30 m. Figure 10 demonstrates the expected pixel temporal profile of the scattered back control signal (notice that the signal scattered back in air produces a continuous curve). The response of all pixels to one flasher pulse yields 3D information on the atmosphere in the detector FOV.

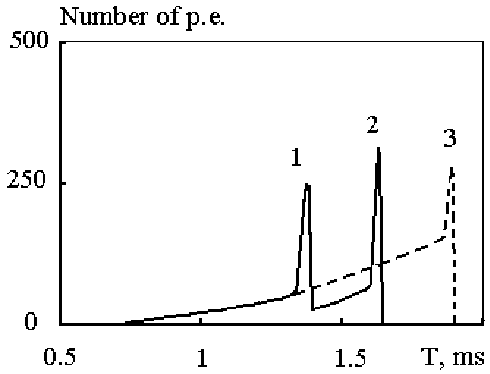

Fig. 10. The temporal profile of the flash lamp signal scattered back from the atmosphere: 1 — the light scattered from semitransparent upper clouds, 2 — the light scattered from clouds, 3 — the light scattered from ground

Due to the large mirror area, the level of signals in Figure 10 is large (10–100 times larger than the noise in a time interval of 200 ns) even from a comparatively low intensity flash: in the KLYPVE detector, the flash pulse power should be about 0.1 J and, in the TUS detector, it is $\approx$ 1 J. Lamps of that luminosity are available in the range of wavelength 350–400 nm, where the photo receiver sensitivity is high. Measuring the "reflected" signal for a known lamp luminosity, it is possible to determine the combined factor $k\eta$, where k is the "albedo" coefficient of media and η is the light absorption coefficient in the atmosphere. With a known factor $k\eta$, the RChS of the EHECR event could be used as an additional estimator of the primary energy (along with the measure of fluorescent signals).

In the case when the RChS is out of the camera FOV, an estimate of the absolute depth $X_{\max}$ could be done in an analysis of the track profile. The fluorescence track length depends on the depth in the atmosphere (on the air density), since the EAS development is invariant in units of g/cm^2 and the fluorescence yield is invariant in geometrical units. The scattered Cherenkov light also depends on the air density: the lower in atmosphere is the track, the higher portion of the scattered Cherenkov light will be detected. For neutrino-induced horizontal tracks uniformly distributed with depth in the atmosphere, both effects will make the track profile variable with depth. The two expected "experimental" horizontal track profiles are represented in Figure 11: for $H = 4$ km and $H = 1.5$ km. At the height $H = 4$ km, the fluorescence track is almost twice longer due to a difference in the air density. In the same shower, the ratio between the Cherenkov scattered light and the fluorescence light is higher for lower values of H. Each of the parameters (the length of the track and the "tail" of the Cherenkov scattered light) may be an indicator of a shower position in the atmosphere even when the information on a RChS is not available.

5. Data analysis. Expected errors in energy and direction of primary particles. EHECR track data allow us to determine the main parameters of a primary particle: the energy E_0, the directional angles θ (zenith) and φ (azimuth), and a position of the shower maximum $X_{\max}$. The PMT charge in each pixel or the charge in a given time interval (when one pixel is considered) corresponds to the flux $Q_{\max}$ of the fluorescence light emitted in a given track length interval ΔL (formula (2.3), Section 2). In the first approximation, the primary energy could be determined from the flux Q at the shower maximum. $Q_{\max}$ is determined not only by the pixel with the maximum signal but from the cascade curve available from all hit pixels. The statistical accuracy in $Q_{\max}$ (in p.e.) is better than 10 %, even at an energy threshold of the detector. An error in the primary energy is caused by the uncertainty in the light accumulation at each pixel in a real mirror and by the uncertainty in experimental measurements of the pixel signals.

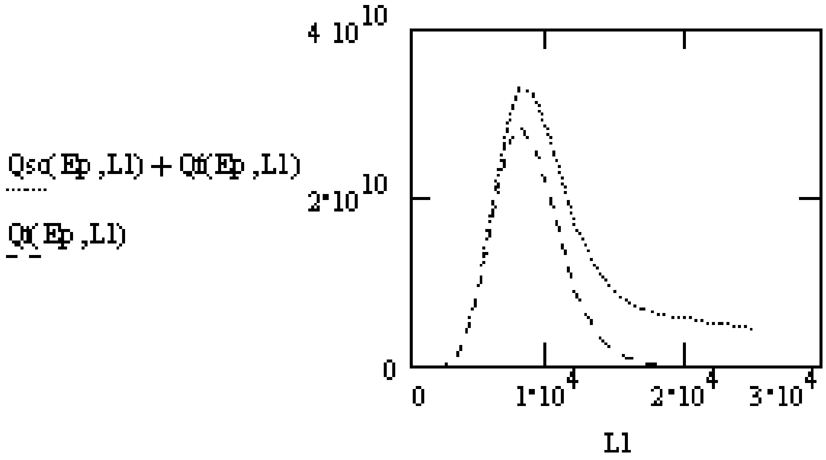

$H = 1.5\ km$

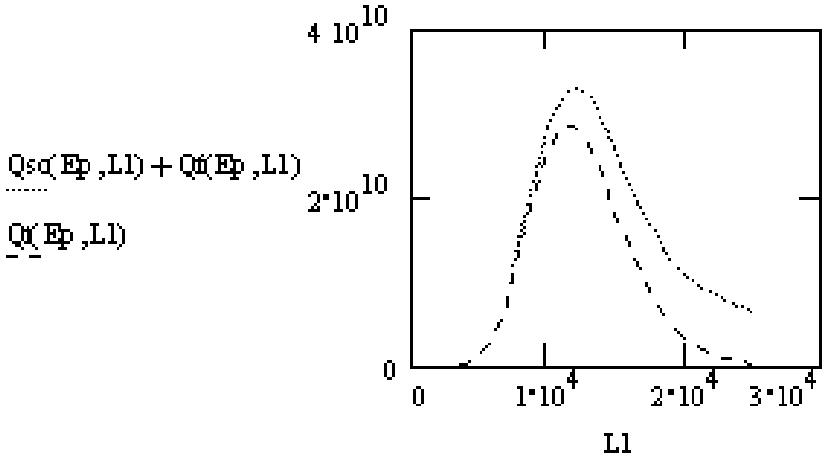

$H = 4$ km

Fig. 11. The horizontal track profiles for the two levels of depth in the atmosphere: $H = 1.5$ km, $H = 4$ km.

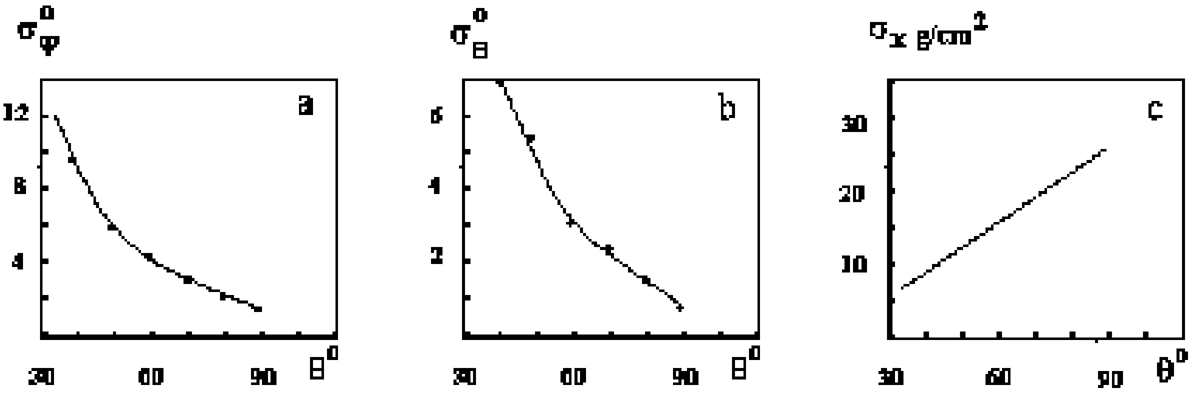

a *b* *c*

Fig. 12. Errors in the azimuth angle (a), in the zenith angle (b), and in a position of the shower maximum (c) as a function of the zenith angle

The determination of the directional angles θ and φ could be done by an analysis of timing of the track at pixels with given coordinates, i.e., at given angular coordinates of the track. According to this method, a square pixel shape is preferable. Summing data of the "hit" neighbor square pixels in both orthogonal directions, one can determine the instant of time when the track crosses the pixel orthogonal coordinates. The azimuth angle is determined from the ratio of the track durations in the two orthogonal directions:

$$\tan\varphi = \Delta t_x/\Delta t_y \tag{5.1}$$

A position in time of the RChS could be added to this analysis; the accuracy in the azimuth angle is higher when a RChS is available. When the zenith angle decreases, the number of the "hit" pixels decreases and an error in the angle φ increases. The estimate of an error in the angle φ as a function of the zenith angle is represented in Figure 12 *a* for the KLYPVE detector ($E_0 = 3\cdot 10^{19}$ EeV).

The zenith angle θ is determined by an analysis of the angular velocity of the track. The following relation is valid at the center of the detector FOV:

$$\Delta\psi/\Delta t = c\sin\theta/R\big(1+\cos\theta\big) \tag{5.2}$$

Here $\Delta\psi$ is the angular size of the track in the pixel plane and Δt is the duration of the track in this angular size. It is evident that the error in the zenith angle increases when the zenith angle decreases (the number of "hit" pixels decreases). As in the case of the azimuth angle, the RChS is helpful for more the precise determination of the zenith angle. Errors in the zenith angle are shown in Figure 12 *b* as a function of θ.

The important parameter of the shower is a position of the shower maximum $X_{\max}$. As mentioned above, the measurement of the RChS with a known height in the atmosphere yields a reference height (depth) in the atmosphere for the whole track. The reference height might be measured with high accuracy (30 m). The precision in a position of $X_{\max}$ is limited due to an error in the relative position of $X_{\max}$ of the track. For inclined tracks ($\theta > 60°$), the position of the maximum could be determined with an error much less than the pixel size ($\ll 40$ g/cm^2). For near-vertical tracks, $X_{\max}$ is determined from the temporal profile of the track with an accuracy dependent on the timing accuracy. If the profile is measured in time intervals 1 μs then the relative position of $X_{\max}$ could be determined with an error less than 10 g/cm^2. The resulting absolute position of $X_{\max}$ depends on the zenith angle. It is interesting that big errors in the zenith angle determination in near-vertical showers do not affect the value of $X_{\max}$ determined from the temporal profile of the EHECR event. For near-horizontal showers, the error in $X_{\max}$ increases with increase in errors of the zenith angle. The dependence of errors in $X_{\max}$ on the zenith angle is represented in Figure 12 *c* for the suggested error 10 g/cm^2 in the relative position of the shower maximum.

The above errors were estimated for the KLYPVE detector for the primary energy $3\cdot 10^{19}$ eV as an illustration of the approach chosen to measure the EHECR particle parameters.

6. Design of the KLYPVE and TUS telescopes. In the KLYPVE project, the optical detector ("telescope") for the registration of the EHECR events is planned to be installed aboard the Russian Segment of ISS (RS ISS). A schematic view of the KLYPVE detector together with other parts of the RS ISS is shown in Figure 13.

The telescope mirror is a segmented Fresnel mirror of operation area 10 m^2 with a focal distance of 3 m. The mirror concentrates the light on a pixel mosaic placed in the focal plane. Each pixel has a square window of size 15×15 mm (the angular pixel size is 5 mrad). The camera field of view (15×15 degrees) is filled with the mosaic with 2500 pixels. From the ISS orbit ($R = 400$ km in average), this camera observes the atmosphere area 100×100 km with the pixel resolution 2×2 km.

The shadow of the photo sensor construction is less than 10 % of the mirror area. The transportation of all scientific equipment to the RS ISS will be done by a space vehicle Progress TM that has a limited entrance diameter for transported parts. The design of a segmented Fresnel mirror is suited to this condition. The entire mirror of 37 segments is represented in Figure 14. The diameter of one segment is 60 cm and its thickness is 25 mm. In the lower part of this figure, three segments are shown in a packed state for which the mirror has a size of about 60×100 cm.

The hexagonal shape of the segments was chosen because of the "triangular" mechanical fixing of segments in one plane. Mechanics of the segment development to a full mirror size allows one to make a mirror plane with the segment deflections less than 2 mrad. The Fresnel mirror operation is illustrated in Figure 15 for the example of the first seven mirror segments. The width of reflective rings increases away from the optical axis. The curvature radius of the rings also changes in such a way that the focal point of each ring is in the same position — 300 cm from the mirror plane. The width and the curvature radius of rings are determined by the height of rings that is chosen equal to 10 mm (the base of each segment is 15 mm in thickness). The

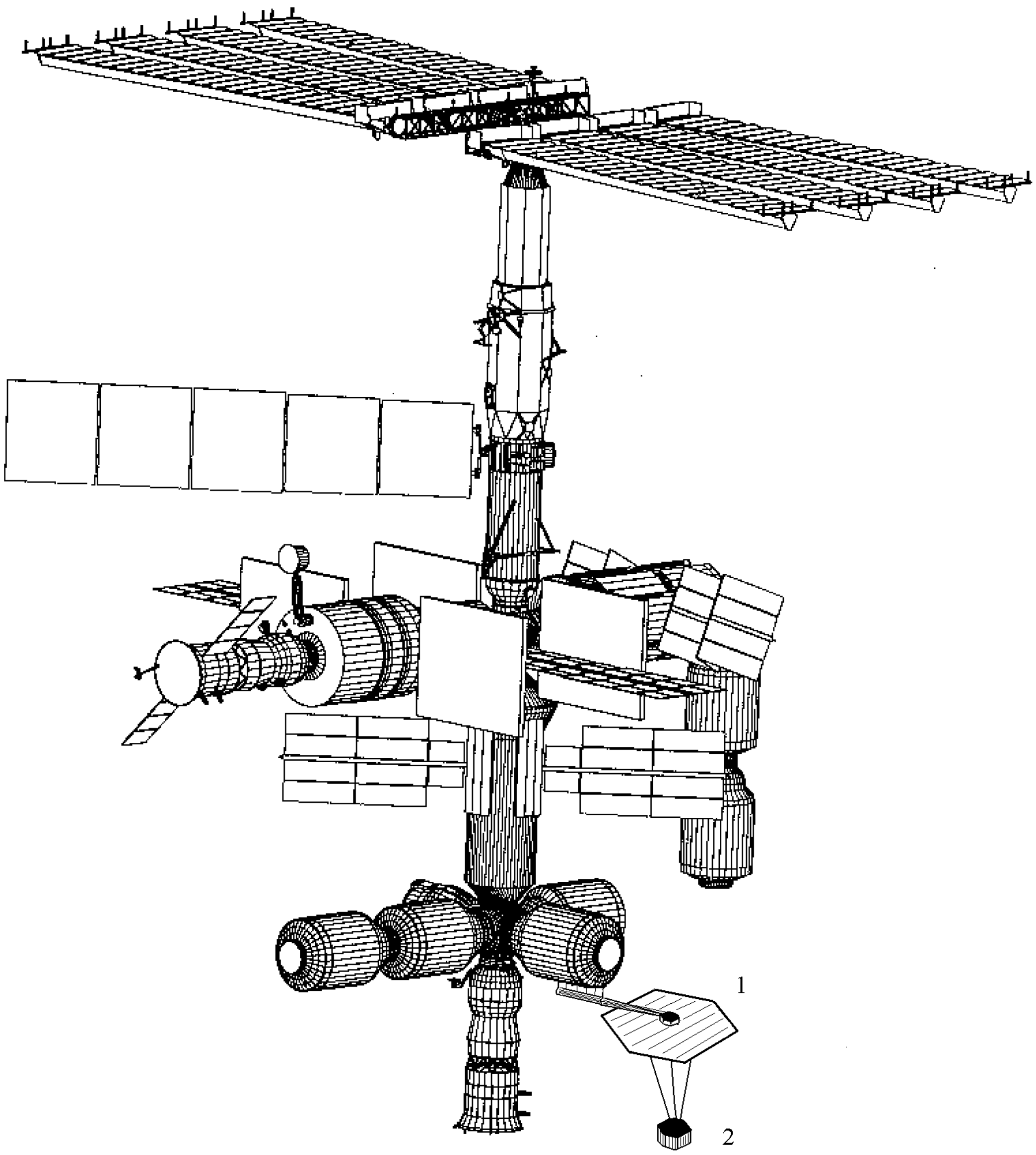

Fig. 13. The schematic view of the Russian segment of the International Space Station with the KLYPVE telescope: 1 — the telescope mirror, 2 — the photo receiver

above-presented mirror segments are supposed to be made of carbon plastic as a replica of the steel polished form shown in Figure 16. The carbon plastic is a special material stable to the temperature changing in a range of $-150° < T < +150°$ C. The carbon surface should be polished and aluminized. The expected reflection coefficient of the aluminized surface is 83 % in the wavelength range 310 – 420 nm.

Fresnel mirror aberrations in the telescope field of view (± 7.5 degrees) was calculated in the Monte–Carlo simulations. It was shown that the Fresnel mirror aberrations are close to parabolic mirror aberrations even when Fresnel rings have the spherical curvature. The photon distribution in the focal plane for a parallel beam with an angle of $7.5°$ to the telescope axis is presented in Figure 17 for a Fresnel mirror and for ordinary spherical and parabolic mirrors of the same diameter and focal distance.

It is evident that the Fresnel mirror operates as a parabolic one. At moderate angles to the optical axis, the aberration in a parabolic mirror is much less than for a spherical one. The aberrations we calculated will be used for the simulation of the EHECR event detection.

The KLYPVE telescope photo receiver is shown in Figure 18. The pixel square windows of light guides allow us to organize an orthogonal network of pixels. PM tubes could be circular with their diameters slightly

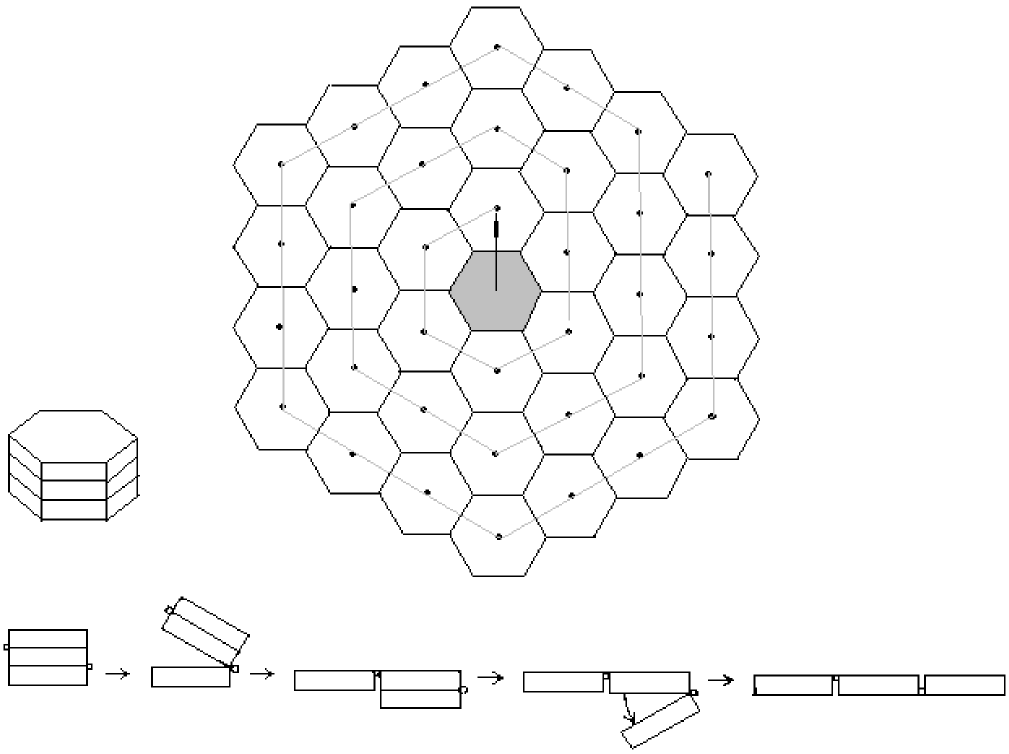

Fig. 14. The KLYPVE mirror of 37 segments. The development from the packed position to the operation position is illustrated for three segments

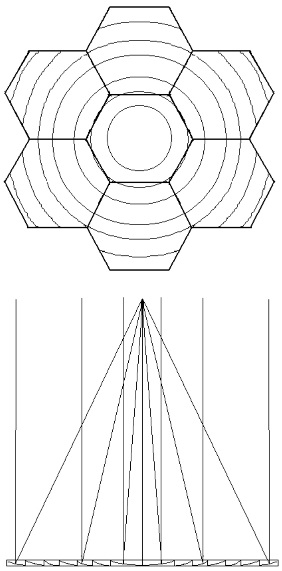

Fig. 15. The illustration of the Fresnel mirror operation (seven segments are shown)

less than 15 mm. The choice of a pixel PM tube is a compromise between the high sensitivity in the fluorescence wavelength band 310 – 420 nm, the stable performance in the presence of high light noise, the fast recovering after exposing to the scattered day atmosphere light, and the slow aging. We prefer to use a tube with a

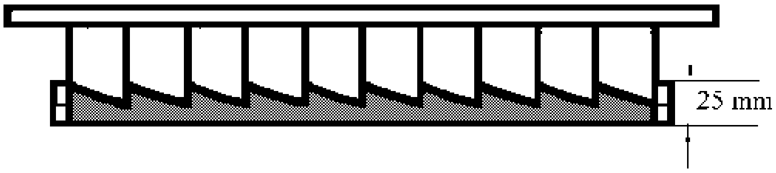

Fig. 16. The carbon mirror replica (the dark area in the figure) of the steel mirror form

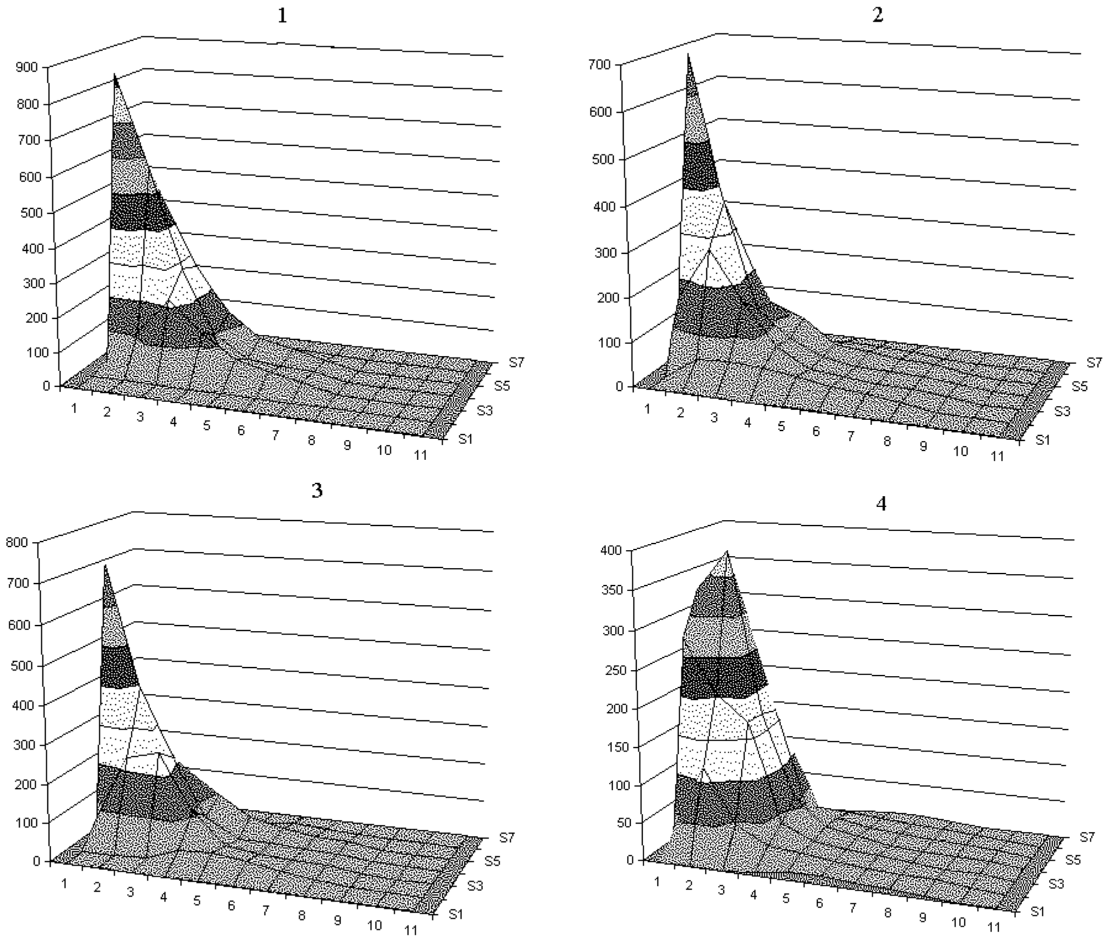

Fig. 17. The photon distribution in the mirror focal plane, $D = 3$ m, $F = 3$ m. The angle to the camera axis is 7.5°. Units in the focal plane are 4 mrad: 1 — the parabolic Fresnel mirror, 2 — the parabolic mirror, 3 — the spherical Fresnel mirror, 4 — the spherical mirror

multialcali cathode and linear dynode system (see [37]). This type of the tube **R 1463P** (13 mm in diameter) is produced by Hamamatsu.

All pixels are covered by a UV filter. A UV window and an insulation box form a pressurized container for the pixel tubes, pixel electronics, and data acquisition system. Event data has to be sent to the RS ISS-mounted computer and, then, to the mission center on the Earth.

The time schedule of the KLYPVE project depends on the time schedule of the RS ISS development (the preliminary launching date is 2006–2007). As a pilot experiment in line of the KLYPVE project, the TUS experiment is planned on one of the Russian satellites (Resurs DK1) scheduled for launching earlier: in 2004.

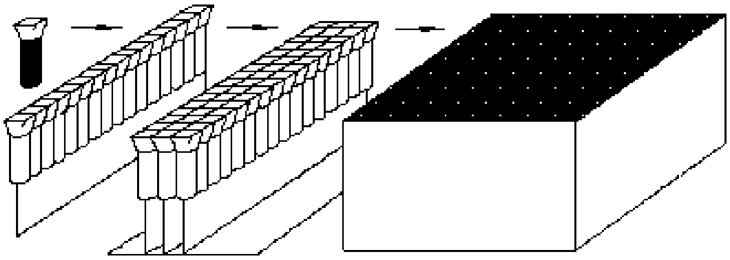

Fig. 18. The telescope photo receiver (from left to right: one pixel — a pixel raw — a box of pixels and electronics)

The TUS equipment is limited in mass and energy consumption, since it is a small addition to the main Resurs DK1 payload. In limits of the Resurs conditions, the TUS telescope has parameters presented above in Section 3, Table 3.1. The TUS mirror and photo receiver have to be transported to an orbit in a packed form and will be developed to their full size as shown in Figure 19.

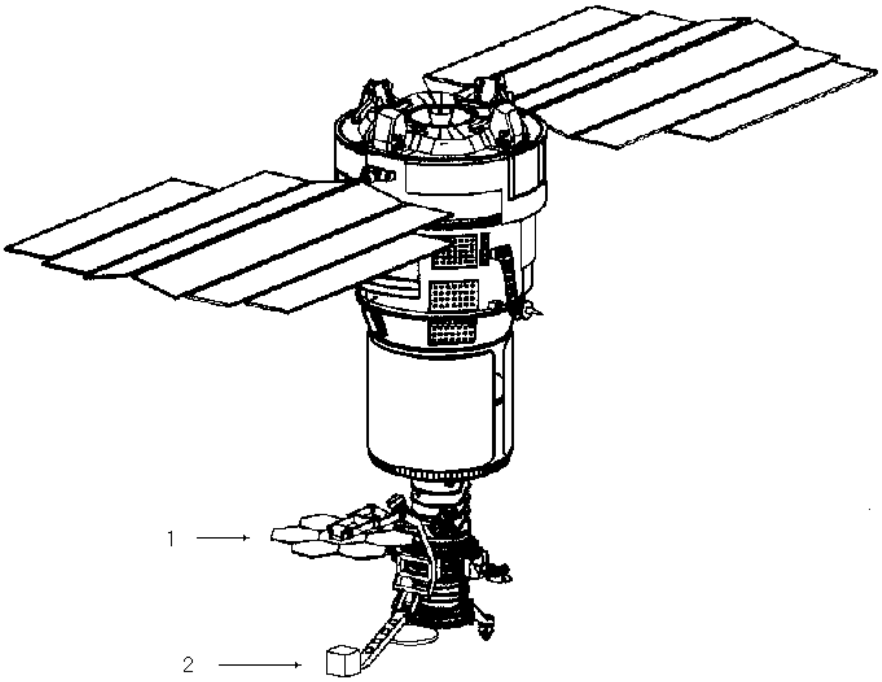

Fig. 19. The TUS telescope on the Resurs DK1 satellite: 1 — the telescope mirror, 2 — the photo receiver

The TUS telescope will measure the light noise under various conditions and will monitor the atmosphere, clouds, ground and sea by receiving the back scattered light from the flasher. The scientific program of the TUS experiment is not as wide as that of the KLYPVE experiment, but any information on the EHECR events in the energy range $10^{19} - 10^{20}$ eV is valuable.

7. Expected scientific results from the TUS telescope. The first expected scientific result from the TUS experiment is a shape of energy spectrum of the EHECR events. With a precision of 10 % in the energy determination (higher than for ground arrays: 30 % in AGASA), there is a chance to resolve the spectrum

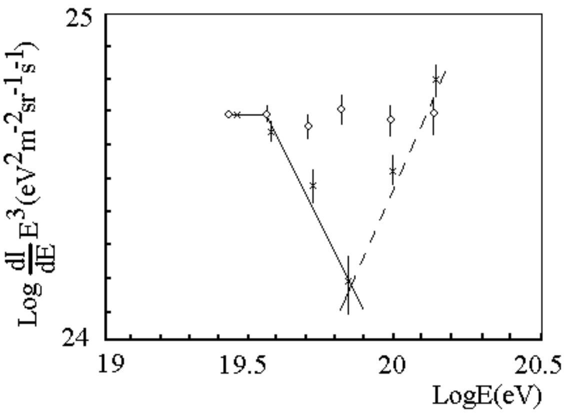

Fig. 20. An expected cosmic ray energy spectrum in three years of the TUS telescope operation. The crosses correspond to the spectrum with a cut-off (the solid line) and a new cosmic ray component (the dashed line) as the AGASA data indicated. The open circles correspond to the power law spectrum

structure in the practically interesting range of 30 – 100 EeV, where the AGASA data indicated the cut-off at $5 \cdot 10^{19}$ eV and a new EHECR component at higher energies. Assuming that a cut-off exists, from AGASA data we found (taking into account their energy resolution of 30 %) the real cut-off shown in Figure 20 by the solid line.

After three years in operation, the TUS telescope will allow us to resolve the energy spectrum structure in the range between $3 \cdot 10^{19}$ and 10^{20} eV. The expected TUS data are shown in Figure 20: crosses correspond to the existing structure and circles correspond to the energy spectrum of a power law with exponent 3.

The expected statistics of events with $E_0 > 10^{20}$ eV (of about 100 events in three years) will allow us to search for the EHECR point sources. If a point source is revealed, the composition of particles in the source will be studied via measurements of the angular distribution of particles that belong to the source.

Another interesting result is the distribution over $X_{\max}$ of all registered events. In Figure 4 (Section 2), this distribution is shown for proton-nuclei cosmic ray particles (the central main bulk of events), for relativistic grains (the left distribution), and neutrinos (the right shaded area). The first registration of events beyond the usual proton-nuclei components of cosmic rays will be an important discovery. The registration of neutrino events will open a new direction of the experimental EHECR research. The EHE neutrino “astronomy” is one of the interesting goals of the Kosmotepetl space program.

8. Summary. In order to extend the EHECR observation to energies up to 10^{21} eV, the observed Earth's atmosphere area has to be much larger than area available for the now existing land-based arrays. The use of the Earth's atmosphere in a global scale as a huge target for the EHECR particles including EHE neutrinos is a new perspective to be opened by space optical detectors. In the Kosmotepetl space program, the first detectors (the KLYPVE telescope on the RS ISS and its prototype: the TUS telescope) will start to observe a moderate atmosphere area (10,000 km^2). In future, larger and more remote telescopes will observe areas comparable to the area of the Earth.

The method of “downward” EHECR observations has been evaluated in model calculations that proved the advantages of space-based optical detectors of the “telescope” type. The final design of the TUS and KLYPVE telescopes will be checked in more extended model calculations.

REFERENCES

1. J. Linsley, *Phys. Rev. Letters*, **10**: 146, 1963.
2. G.T. Zatsepin and V.A. Kuzmin, *JETP Letters*, **4**: 78, 1966.
3. K. Greisen, *Phys. Rev. Letters*, **16**: 748, 1966.
4. J.W. Elbert and P. Sommers, *Astrophys. J.*, **441**: 151, 1995.
5. C.J. Cesarsky, *Nucl. Phys. B* (*Proc. Suppl.*), **28**: 51, 1992.
6. M. Takeda et al., *Astrophys. J.*, **522**: 225, 1999.
7. A.M. Hillas, *Ann. Rev. Astron. Astrophys.*, **22**: 425, 1984.

8. P. Bhattacharjee and G. Sigl, *Phys. Rep.*, **327**: 110, 2000.

9. J. Learned and K. Mannheim, *Ann. Rev. Nucl and Part. Sci.*, 2000.

10. G.B. Khristiansen et al., 14-th Texas Symp. on Rel. Astrophys., Ann., N-Y Ac. Sci., **571**: 640, 1987.

10. G.B. Khristiansen et al., *Nucl. Phys.* (*Proc. Suppl.*), **B 28**: 40, 1992.

11. Staged Construction Proposal for the High Resolution Fly's Eye (HiRes) Detector. September 10, 1993.

12. J. Cronin, *Nucl. Phys.* (*Proc. Suppl.*), **B 28**: 213, 1992.

13. The Pierre Auger Project. Design Report, 1995 (1-st edition), 1996 (2-nd edition).

14. Telescope Array Collaboration, *Proc.* 23-*d ICRC*, Durban, **5**: 369, 1997.

15. J. Linsley and R. Benson, *Proc.* 17-*th ICRC*, Paris, **8**: 145, 1981.

16. J. Linsley], *Proc.* 23-*d ICRC*, Durban, **1**: OG 10.6.19, 1997.

17. G.K. Garipov, L.A. Gorshkov, B.A. Khrenov et al., *Proc. of Workshop on Observing of Giant Cosmic Ray Air Showers from* $> 10^{20}$ *eV Particles from Space, AIP Conf. Proc.*, Woodbury, N.Y., **433**: 108, 1998.

18. G.K. Garipov, B.A. Khrenov, V.P. Nikitsky et al., *Ibid., AIP*, **433**: 403, 1998.

19. R.E. Streitmatter et al., *Ibid., AIP*, **433**: 95, 1998.

20. L. Scarsi et al., *Extreme Universe Space Observatory* (*EUSO*) *Proposal for the ESA F2/F3 Missions*, 2000.

21. V.V. Alexandrov et al., *Vestnik MSU. Astronomy. Physics*, 6: 33, 2000.

22. V.V. Alexandrov et al., *Proc. of Workshop on Observing of Extremely High Energy Cosmic Ray from Earth and Space, AIP Conf. Proc.*, Woodbury, N.Y., in press, 2001.

23. D.J. Bird et al., *Proc.* 23-*d ICRC*, Rome, **2**: 38, 1993.

24. F.A. Aharonian, B. L. Kanevsky, and V.A. Sahakian, *J. Phys. G: Nucl. Part. Phys.*, **17**: 1909, 1991.

25. S. Karakula and W. Bednarek, *Proc. of the* 24-*th ICRC*, Rome, **1**: 266, 1995.

26. X. Bertou and P. Billoir, *Auger GAP* 99006, 1999.

27. N.N. Kalmykov et al., *Nucl. Phys. Russian*, **58**: 1829, 1995.

28. L. Spitzer, *Phys. Rev.*, **76**: 583, 1949.

29. S. Hayakava, *Astrophys. Space Sci.*, **16**: 238, 1972.

30. V.S. Berezinsky and O.F. Prilutsky, *Astrophys. Space Sci.*, **21**: 475, 1973.

31. R. Bingham and V.N. Tsytovich, *Astroparticle Phys.*, **12**: 35, 1999.

32. T. Stanev, *Talk at the Auger meeting*, May 1997.

33. N.P. Iljina, N.N. Kalmykov, and V.V. Prosin, *Nucl. Phys. Russian*, **55**: 2756, 1992.

34. A.I. Lebedinsky et al., *Space Research* (in Russian), Moscow, 1965.

35. R.M. Baltrusaitis et al., *NIM*, **A 240**: 410, 1985.

36. S.N. Kuznetsov et al., *European Symposium on Cosmic Rays*, oral presentation, 2000.

37. S.A. Beljanchenko et al., *Preprint INP MSU* (in Russian), Moscow, 1998.